**Supplementary Information**

# Conversion of Novel Bimetallic Metal Organic Frameworks into Hierarchically Structured Electrocatalysts for High Performance Hydrogen Evolution

Dhouha Abid, [a] Soressa Abera Chala, [a] Rongji Liu, [a] Tobias Rios-Studer, [a] Christean Nickel, [a] Sarra Rahali, [a] Kevin Sowa, [a] Galina Matveeva, [a] Dandan Gao, [a] Ute Kolb, [a] and Carsten Streb [*a]

[a] Department of Chemistry, Johannes Gutenberg University Mainz, Duesbergweg 10-14, Mainz 55128, Germany.

## Table of Contents

# 1. Materials and Methods

## 1.1. Chemicals

All chemicals were used as received without further purification: cobalt(II) nitrate hexahydrate ($Co(NO_3)_2 \cdot 6H_2O$, 98%, Sigma-Aldrich), Nickel (II) nitrate hexahydrate ($Ni(NO_3)_2 \cdot 6H_2O$, 98.5%, Sigma-Aldrich), 4,4′-bipyridine ($C_{10}H_8N_2$, 98%, TCI), and (1R,3S)-(+)-camphoric acid ($C_{10}H_{16}O_4$, 99%, Thermo Fisher Scientific).

## 1.2. Instrumentation

**Scanning electron microscopy (SEM):** Scanning electron microscopy was performed on a Hitachi 5200 equipped with an EDX detector.

**Scanning transmission electron microscopy (STEM):** Phase contrast TEM, scanning TEM (STEM), and fast automated diffraction tomography (Fast-ADT) analyses were performed using a Tecnai F30 S-TWIN TEM, equipped with a field emission gun and operated at 300 kV. The setup included a 10 mm condenser aperture, gun lens set to 8, and a spot size of 8. For electron diffraction pattern acquisition, the beam diameter was adjusted to 50 nm. TEM images were recorded using a 4k × 4k Gatan US4000 CCD camera (Gatan, Pleasanton, USA) with a hardware binning of 2.

Fast-ADT diffraction data were acquired using an automated module designed for FEI and JEOL microscopes, enabling high-angular-range tomography (up to 140°) within approximately 5 minutes for TIMEPIX cameras, with a fixed tilt step of 1°. The crystal position was monitored in microprobe STEM mode, and electron diffraction patterns were obtained under the same conditions. Fast-ADT series were automatically collected over a tilt range of -50° to 50°, with a 1° step and an exposure time of 0.1 seconds per frame. To integrate reflection intensities across the tilt wedge experimentally, Fast-ADT was combined with precession electron diffraction (PED), generated by a NanoMEGAS DigiStar unit, maintaining a beam precession angle of 1°.

**FT-Infrared spectroscopy (FT-IR):** FT-IR analysis was performed at room temperature using a Bruker Tensor 27 spectrometer, equipped with a diamond attenuated total reflectance (ATR) unit, spanning the frequency range of 400-4000 $cm^{-1}$.

**Thermogravimetric analysis (TGA):** Thermogravimetric analysis was performed on 5 mg of powdered sample using a Mettler Toledo system. The measurements were conducted under air atmosphere, with the temperature increasing from 30.00 to 450.00 °C at a rate of 5.00 °C/min.

**Single crystal X-ray diffraction (SC-XRD) measurements:** For the crystal structure determination, X-ray diffraction intensity data for the as-prepared CoNi-MOF was collected on a STOE IPDS 2T diffractometer using Mo-Kα radiation. Data were collected at 293 K (2) over $1.9^\circ \leq \theta \leq 32.9^\circ$. A total of 20923 reflections were recorded

with 4603 showing intensities of $I>2\sigma(I)$. The crystalline structure was solved in the monoclinic crystal system with the $P2_1$ space group. Cobalt and nickel atom positions were identified using the Patterson method within the WINGX software. [1] Remaining atoms (carbon, oxygen, and nitrogen) were located via successive Fourier calculations and refined with anisotropic thermal parameters using SHELXL-2018. [2] Pore volume was calculated using PLATON SQUEEZE software. Full experimental details for the CoNi-MOFs are summarized in **Table S1**.

**Powder X-ray diffraction (PXRD):** Powder X-ray diffraction was carried out using a Bruker AXS D8 Advance system with Cu Kα radiation (λ = 1.5406 Å) at 40 kV and 40 mA.

**Nitrogen Sorption:** Nitrogen adsorption-desorption isotherms were measured at 77 K using a 3P Micro 300 Surface Area and Pore Size Analyzer to characterize the surface area and pore size of the materials. Prior to analysis, samples were degassed under vacuum. The as-prepared MOF precursors were degassed at 80 °C (353 K) for 20 hours, while the calcined catalysts were degassed at 200 °C (473 K) for the same duration. Nitrogen gas was used as the adsorbate. Pore size distributions were calculated using the Barrett-Joyner-Halenda (BJH) method with a KJS correction.

**X-ray photoelectron spectroscopy (XPS):** X-ray photoelectron spectroscopy was conducted using monochromatized Al Kα X-ray radiation with a PHI Quantera SXM system. The binding energies were calibrated with reference to the C 1s peak at 284.8 eV.

**X-ray absorption spectroscopy (XAS):** X-ray absorption spectroscopy (XAS) measurements were performed using a lab-based hiXAS system with EXAFS mode. A quick-scanning extended X-ray absorption fine-structure (QEXAFS) approach was employed in transmission mode, enabling efficient data acquisition with a monochromator oscillation frequency of 1 Hz. The acquisition time was 10 minutes for Ni and Co foil reference standards, and 3 hours for the other samples. Prior to analysis, all samples were pressed into 15 mm diameter pellets. The XAS data were analyzed using Athena and Artemis software. [3]

**Inductively coupled plasma optical emission spectrometry (ICP-OES):** ICP-OES was performed using a Perkin Elmer Plasma 400 spectrometer. Measurements were conducted in an aqueous $H_2SO_4$-$HNO_3$ solution.

### 1.3. Electrochemical Measurements

**Preparation of the Working Electrode:** The fabrication of the working electrode is a crucial step in assessing the electrochemical properties and practical applicability of the synthesized catalysts. To prepare the catalyst ink, 5 mg of the calcined Co, Ni and CoNi-MOF catalyst was dispersed in a mixture containing 900 µL of isopropanol, 50 µL of deionized water, and 50 µL of Nafion solution (5 wt.% in a lower alcohol mixture). The suspension was sonicated for 1 hour to ensure uniform dispersion. For electrode preparation, 13 µL of the ink was drop-cast onto a glassy carbon electrode (GCE), or

100 µL was applied onto carbon paper (1 cm² surface area). The modified electrodes were air-dried, achieving a catalyst loading of 0.3 mg·cm⁻².

**Electrochemical measurements** were conducted using an Ametek workstation with PMC-1000 configured in a three-electrode setup. The working electrode was a glassy carbon electrode (GCE) with a disk surface area of 0.196 cm². A Hg/HgO electrode served as the reference electrode, while a graphite rod acted as the counter electrode. The electrolyte used in the experiment was a 1 M aqueous solution of KOH. The hydrogen evolution reaction (HER) activity was evaluated via linear sweep voltammetry (LSV) at a scan rate of 5 mV $s^{-1}$ using a PMC 1000 electrochemical workstation (AMETEK Scientific Instruments). The measured potentials were referenced to the reversible hydrogen electrode (RHE) using the Nernst equation:

$$E_{RHE} = E_{Hg/HgO} + E^{0}{}_{Hg/HgO} + 0.0592\ V \times pH$$

Polarization curves were recorded without iR compensation, and the Tafel slope was determined using the Tafel equation:

$$\eta = a + b \log(j)$$

Here, j represents the current density, which was normalized to the geometric surface area of the GCE. For long-term stability assessments, the catalyst was supported on carbon paper (~1 cm²).

**Electrochemically Active Surface Area (ECSA):** The ECSA of the catalysts was estimated by evaluating the electrochemical double-layer capacitance (Cdl) through cyclic voltammetry (CV) in the potential window of 0.08 V to 0.1 V, where no faradaic processes occur. To ensure signal stability, multiple cyclic scans were performed before data collection.

**Electrochemical Impedance Spectroscopy (EIS):** EIS measurements were conducted at 1.55 V vs. RHE with a 5 mV AC perturbation, sweeping frequencies from 100 kHz to 0.01 Hz. The impedance spectra were analyzed using Z view software by fitting the data to an appropriate equivalent circuit model.

**Faradaic efficiency:** Hydrogen production was quantified using gas chromatography (Shimadzu GC-2030) equipped with a barrier ionization discharge (BID) detector. High-purity helium (He, 99.999%) served as the carrier gas. The faradaic efficiency was determined using the following equation:

$$FE_i = \frac{\alpha_i n_i F}{Q} x100\%$$

Where; $\alpha_i$ represents the number of electrons needed to generate one hydrogen molecule, $n_i$ denotes the number of moles, $F$ is the Faraday constant (96,485 C $mol^{-1}$), and $Q$ corresponds to the total electric charge transferred during the experiment.

### 1.4. Flow-cell measurements:

**Preparation of the Working Electrode:** For the flow-cell experiments, the catalyst ink was prepared following the same procedure described above. The ink was drop-cast onto carbon paper with a geometric area of 2 $cm^2$ and dried at room temperature. After solvent evaporation, the catalyst loading at the cathode was adjusted to 0.6 mg $cm^{-2}$.

**Flow-cell measurements:** An anion exchange membrane (AEM) electrolyzer was assembled using a sandwich-type configuration. The coated carbon paper (2 $cm^2$, 0.6 mg $cm^{-2}$ loading) served as the cathode, while commercial Ni foam was used as the anode. Current collectors were employed on both sides, and an AEM (pre-activated in 1 M KOH) was positioned between the electrodes. The cell was operated using 1 M KOH electrolyte, which was continuously circulated through the flow channels via a peristaltic pump to ensure efficient electrolyte renewal and minimize concentration gradients during operation. Before polarization measurements, the cell was conditioned under open-circuit conditions at 70 °C for 30 min. Polarization curves were subsequently recorded under steady-state conditions, followed by long-term electrolysis at a constant current density of 200 mA $cm^{-2}$ to assess the stability of the catalyst.

## 2. Experimental section

### 2.1. Synthesis

**Synthesis of monometallic Co-MOF Precursor**

To synthesize the monometallic Co-MOF, an aqueous solution of $Co(NO_3)_2 \cdot 6H_2O$ (291 mg, 1 mmol) was gradually added to a mixture of D-camphoric acid (10 mg, 0.5 mmol) and 4,4′-bipyridine (79 mg, 0.5 mmol) in N,N-dimethyl formamide (DMF) under continuous stirring at room temperature. The solution was then neutralized with 0.1 M aqueous KOH, followed by microwave-assisted heating at 70 °C for 35 min under an autogenous pressure of 2 bar. The resulting pink, needle-shaped crystals were thoroughly washed with water, ethanol, and DMF three times, and air-dried at room temperature. The synthesized MOF was activated under vacuum at 80 °C for 4 h to remove the solvent molecules trapped in the pores of the MOF framework. This activation yielded the pure MOF with a 57% in yield. FT-IR spectra ($cm^{-1}$, with their corresponding intensities (s = strong, m = medium, w = weak): 3260 (w), 2961 (m), 2885 (w), 1610 (w), 1542 (s), 1410 (s), 855 (s), 465 (m).

**Synthesis of monometallic Ni-MOF Precursor**

For the monometallic Ni-MOF synthesis, the same protocol was followed, except that a mixture of $Ni(NO)_2 \cdot 6H_2O$ (7.3 mg, 0.5 mmol) was used. The reaction yielded the purified MOF in 50% yield. FT-IR spectra ($cm^{-1}$, with their corresponding intensities (s = strong, m = medium, w = weak): 3120 (w), 2962 (m), 2820 (w), 1627 (w), 1530 (s), 1462 (s), 870 (s), 463 (m).

**Synthesis of CoNi-dual-doped MOF Precursor**

For the dual-doped CoNi-MOF synthesis, the same protocol was followed, except that a mixture of $Co(NO)_2 \cdot 6H_2O$ (7 mg, 0.5 mmol) and $Ni(NO)_2 \cdot 6H_2O$ (7.3 mg, 0.5 mmol) was used. The reaction yielded the purified MOF in 46% yield. FT-IR spectra ($cm^{-1}$, with their corresponding intensities (s = strong, m = medium, w = weak): 3110 (w), 2952 (m), 2880 (w), 1607 (w), 1540 (s), 1402 (s), 850 (s), 461 (m).

**Synthesis of monometallic Co-MOF catalyst**

The obtained Co-MOF crystals were placed in a quartz crucible and calcined in a tube furnace at temperatures ranging from 550 to 850 °C under a continuous flow of argon for 3 h, with a controlled heating rate of 5 °C/min. After pyrolysis, the resulting oxide sample was thoroughly washed with deionized water and ethanol to remove residual impurities. The final black products were designated based on the calcination temperature: Co-MOF@550 °C, Co-MOF@650 °C, Co-MOF@750 °C, and Co-MOF @850 °C.

**Synthesis of Ni-dual-doped catalyst**

The Ni-MOF crystals were calcined at 850°C under the same conditions, and labeled as Ni-MOF@850 °C

**Synthesis of CoNi-dual-doped catalyst**

The CoNi-MOF crystals were calcined at 850°C under the same conditions, and labeled as CoNi-MOF@850 °C.

## 3. Analytical section

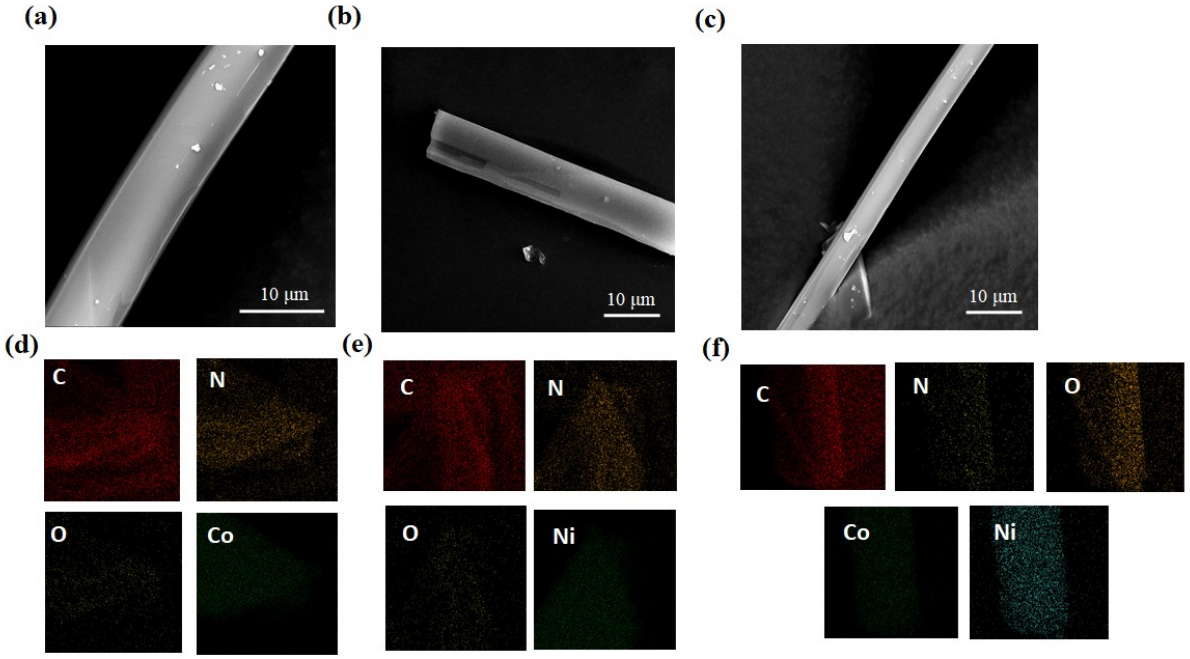


**Fig. S1** SEM images of (a) Co-MOF, (b) Ni-MOF, (c) CoNi-MOF, and (d-f) Corresponding elemental component mappings of Co-MOF, Ni-MOF and CoNi-MOF, respectivelly.

The morphologies of the as-synthesized Co-MOF, Ni-MOF and CoNi-MOF were investigated using scanning electron microscopy (SEM). SEM images of all MOF precursors reveal a distinct needle-like morphology, characteristic of porous structures. In addition, energy-dispersive X-ray spectroscopy (EDX) confirmed the uniform distribution of Co, C, O, and N in the Co-MOF, and Ni, C, O, and N in the Ni-MOF samples and CoNi-MOF showed a homogeneous distribution of Co, Ni, C, O, and N, verifying the successful incorporation of nickel into the framework.

**Table. S1** Experimental details for the as-prepared CoNi-MOF.

| | **CoNi-MOF** |
|---|---|
| Chemical formula | $C_{30}H_{36}(Co/Ni)_2N_2O_{12}$ |
| $M_r$ (g/mol) | 742.53 |
| Crystal system, space group | Monoclinic, $P2_1$ |
| Temperature (K) | 293 (2) |
| a, b, c (Å) | 6.7(6), 13.4(6), 18.5(19) |
| β (°) | 97.5 (8) |
| V (Å$^3$) | 1665.9(3) |
| Z | 2 |
| Radiation type | Mo Kα |
| D | 1.4 |
| Crystal size (mm) | 0.24 × 0.09 × 0.08 |
| No. of measured, independent and observed [I > 2σ(I)] reflections | 20923, 9908, 142 |
| $R_{int}$ | 0.053 |
| R[$F^2$ > 2σ($F^2$)], wR($F^2$), S | 0.086, 0.255, 1.0 |
| No. of reflections | 6116 |
| Flack parameter | -0.016 (1) |

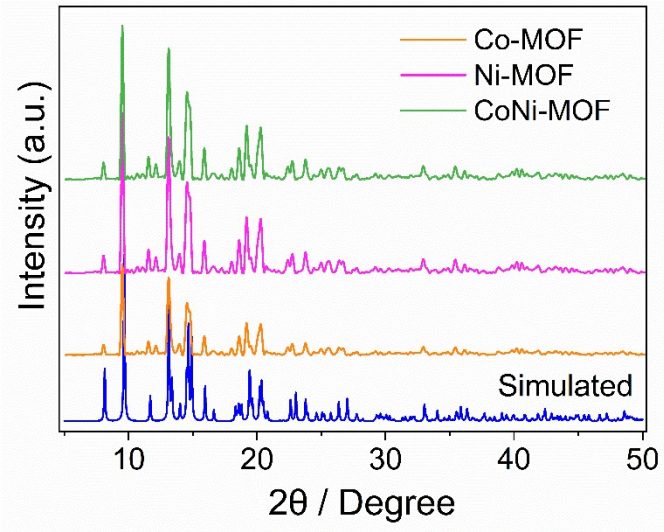


**Fig. S2** The experimental and simulated PXRD patterns of Co, Ni-MOF, and CoNi-MOF.

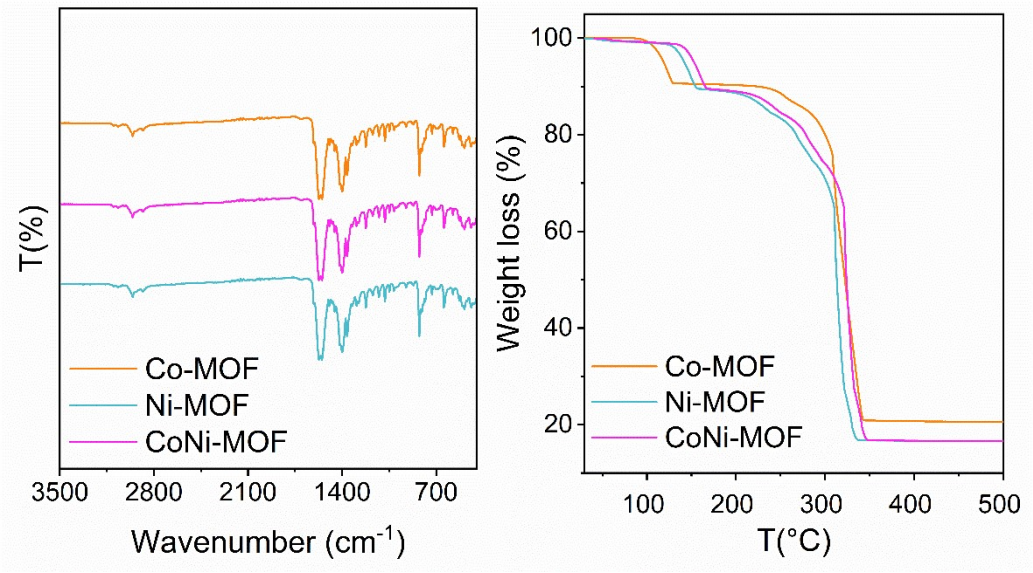


**Fig. S3** (a) FT-IR Spectra of the monometallic Co, Ni-MOF, and bimetallic CoNi-MO, (b) TGA profiles of Co, Ni-MOF, and CoNi-MOF.

The FT-IR spectra of MOF precursors, recorded at room temperature, confirm the removal of guest solvent molecules from the pores after activation (**Figure S2a, SI**). Notable changes in the infrared spectra include a broad band at 3260, 3220 and 3110 $cm^{-1}$ (OH-stretching band), 1610, 168 and 1607 $cm^{-1}$ (H−O−H bending mode), and 850, 851, and 855 $cm^{-1}$, respectively for Co-MOF, Ni-MOF, and CoNi-MOF. After the activation process, both MOFs exhibit similar IR spectra, with characteristic peaks of the organic ligands.

The TGA profiles for porous Co, Ni, and CoNi-MOF (**Figure S2b, SI**) reveal a two-step decomposition process. The initial weight loss, occurring between 80.25 and 129.17 °C for Co-MOF, 81.25 and 140.23 for Ni-MOF and 86.91 and 156.16 °C for CoNi-MOF, corresponds to a 9.49, 9.20 and 9.48 wt%, respectively, attributed to the release of coordinated water molecules. The second stage shows significant weight loss between 184.16 and 341.66 °C for Co-MOF (69.73 wt%), 185.32 and 333.60 °C (68.70 wt%) for Ni-MOF and 190.51 and 335.41 °C for CoNi-MOF (73.57 wt%), associated with the decomposition of the structural framework. This leads to the formation of cobalt oxide (CoO) in the Co-MOF sample, and both nickel oxide (NiO) and cobalt oxide (CoO) as residues in the CoNi-MOF sample.

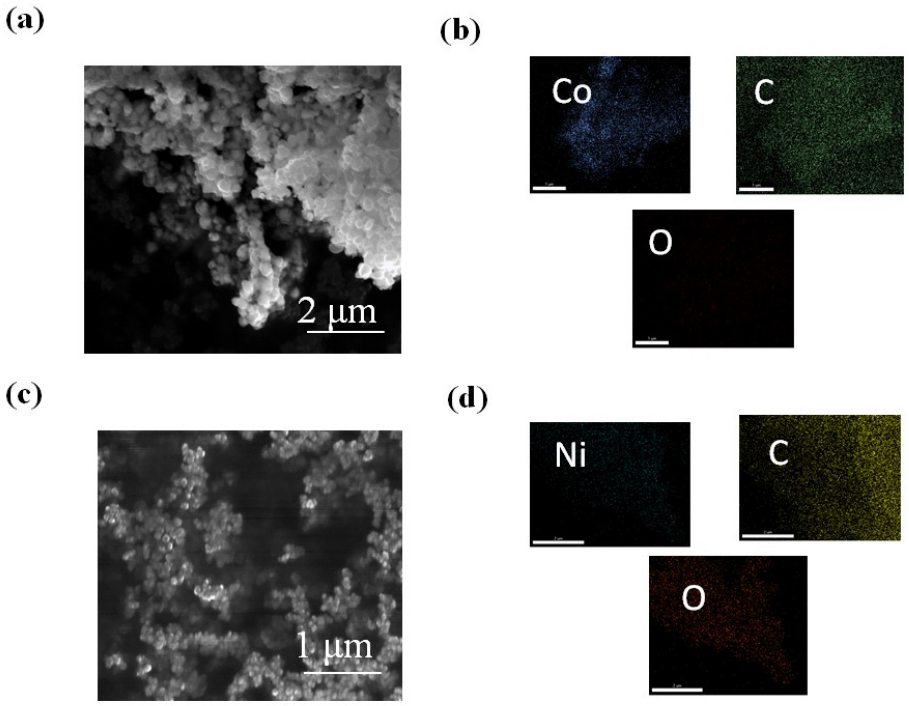


**Fig. S4** (a) SEM images of Co-MOF@850°C, (b) the corresponding pore size distributions of Co-MOF@850°C, (c) SEM images of Co-MOF@850°C, and (d) the corresponding pore size distributions of Co-MOF@850°C.

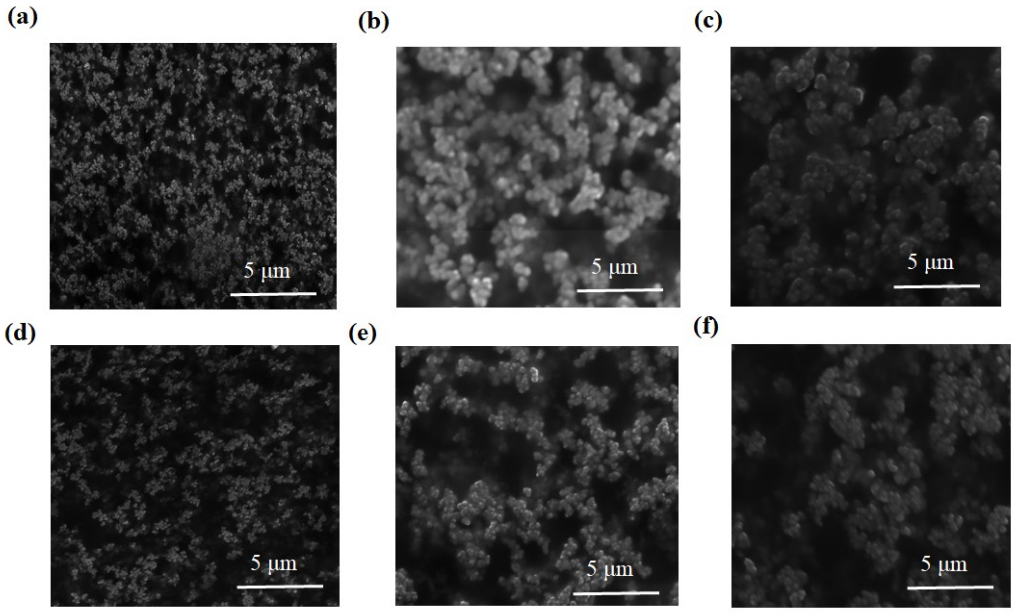


**Fig. S5** SEM images of (a–c) Co-MOF calcined at 550, 650, and 750 °C, and (d–f) Ni-MOF calcined at 550, 650, and 750 °C.

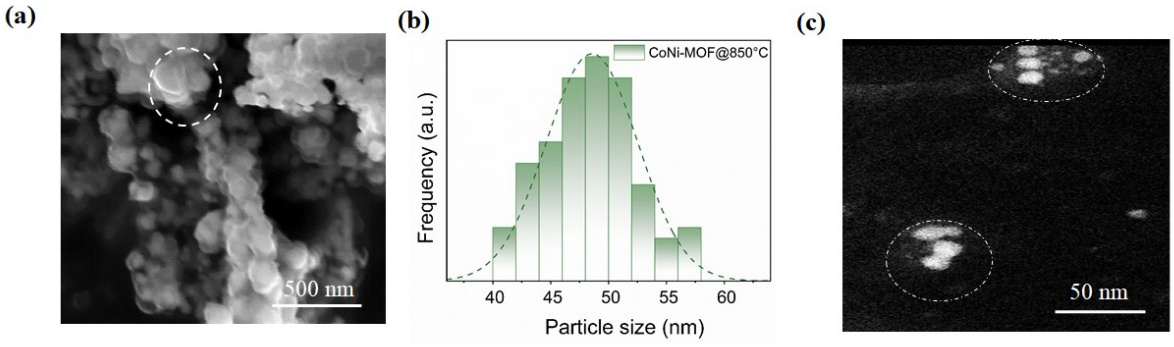


**Fig. S6** (a) SEM image for CoNi-MOF@850°C, (b) particle size distribution histogram, and (c) HAADF-STEM image for CoNi-MOF@850°C.

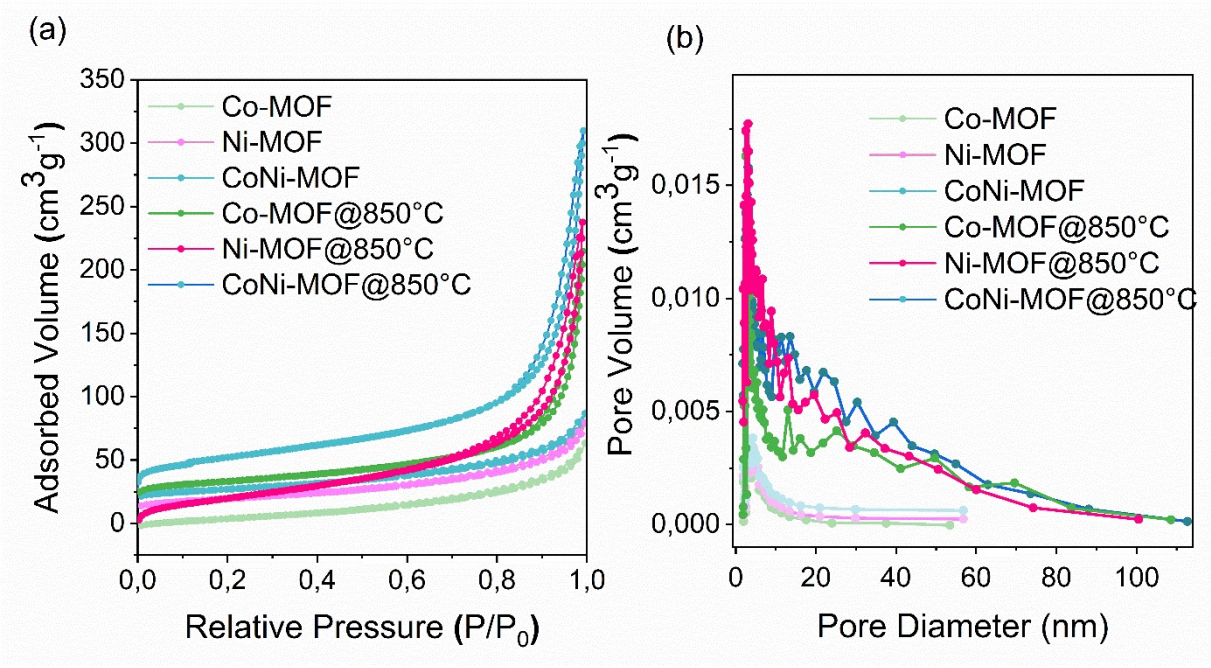


**Fig. S7** (a) Nitrogen adsorption-desorption isotherms of Co, Ni, CoNi-MOF, and Co, Ni, CoNi calcined at 850°C, (b) the corresponding pore size distributions of all samples.

**Table. S2** Specific surface area, pore volume and pore size distribution of Co-MOF, CoNi-MOF, and their calcined forms at 850°C.

| **Material** | **Surface area ($S_{BET}$) $m^2/g$** | **Pore volume ($V_{Tot}$) $cm^3/g$** | **Pore size (BJH) Nm** |
|---|---|---|---|
| Co-MOF | 36.6 | 0.09 | 10.5 |
| Ni-MOF | 41.4 | 0.1 | 11.3 |
| CoNi-MOF | 45.7 | 0.1 | 11.2 |
| Co-MOF@850°C | 124.8 | 0.4 | 14.0 |
| Ni-MOF@850°C | 141.3 | 0.7 | 22.8 |
| CoNi-MOF@850°C | 183.2 | 0.5 | 23.7 |

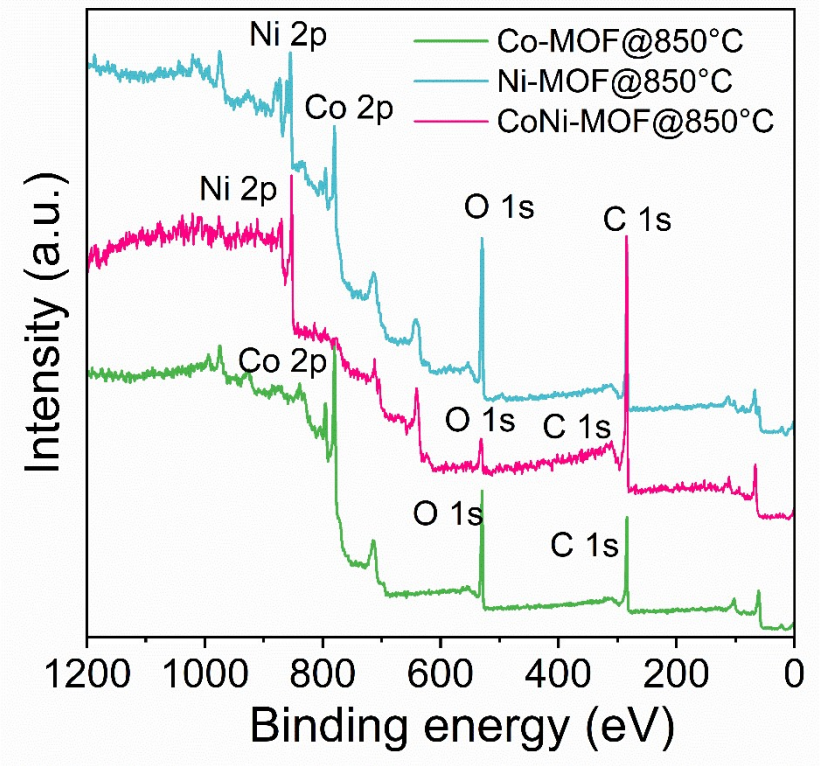


**Fig. S8** XPS survey of Co-MOF@850°C, Ni-MOF@850°C, and CoNi-MOF@850°C catalysts.

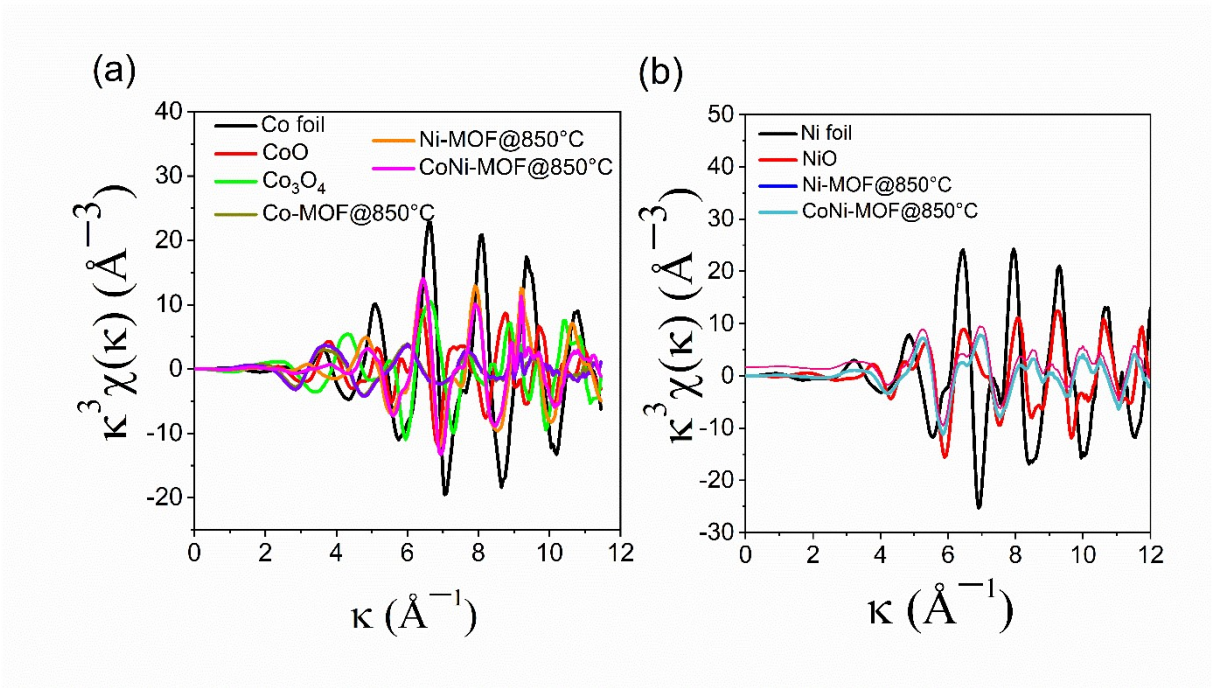


**Fig. S9** (a) Co K-edges, and (b) Ni K-edges of Co, Ni and CoNi-MOFs, and Co, Ni and CoNi- MOF@850°C catalysts along with standard Co and Ni reference materials.

**Table. S3** Metal element contents of the monometallic Co and Ni-MOFs and the bimetallic CoNi-MOF and their calcined catalysts at 850°C determined by ICP-OES.

| **Samples** | **ICP- OES** | |
|---|---|---|
| | Co (wt. %) | Ni (wt. %) |
| Co-MOF | 16.88 | - |
| Ni-MOF | - | 16.03 |
| CoNi-MOF | 9.45 | 7.46 |
| Co-MOF@850°C | 6.14 | - |
| Ni-MOF@850°C | - | 6.01 |
| CoNi-MOF@850°C | 3.73 | 2.52 |

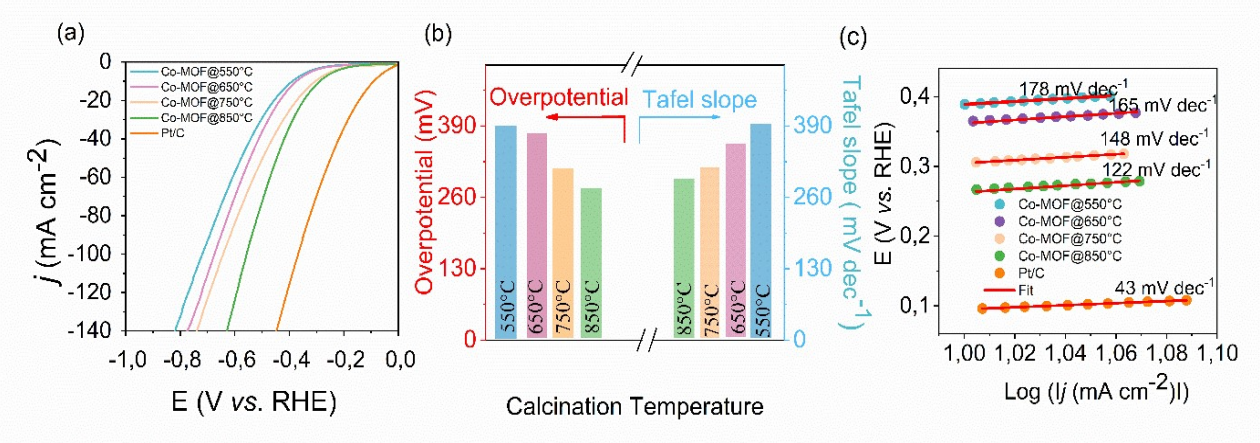


**Fig. S10** Electrocatalytic HER performance of Co-MOF catalysts calcined at different temperatures in 1 M KOH without iR correction: (a) LSV curves, (b) histogram of Tafel slopes and overpotentials at $j$ = 10 mA cm$^{-2}$, and (c) the corresponding Tafel slope plots.

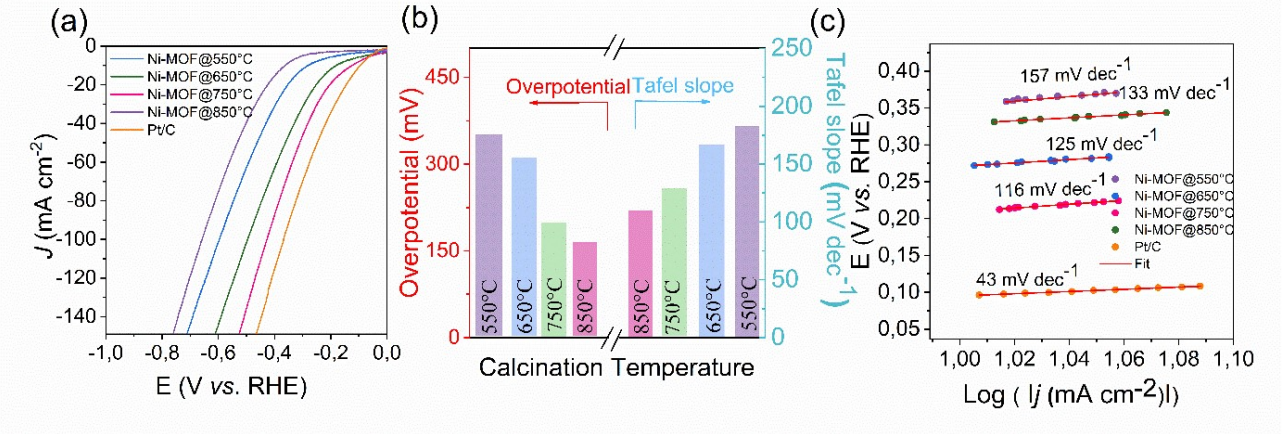

**Fig. S11** Electrocatalytic HER performance of Ni-MOF catalysts calcined at different temperatures in 1 M KOH without iR correction: (a) LSV curves, (b) histogram of Tafel slopes and overpotentials at $j$ = 10 mA cm$^{-2}$, and (c) the corresponding Tafel slope plots.

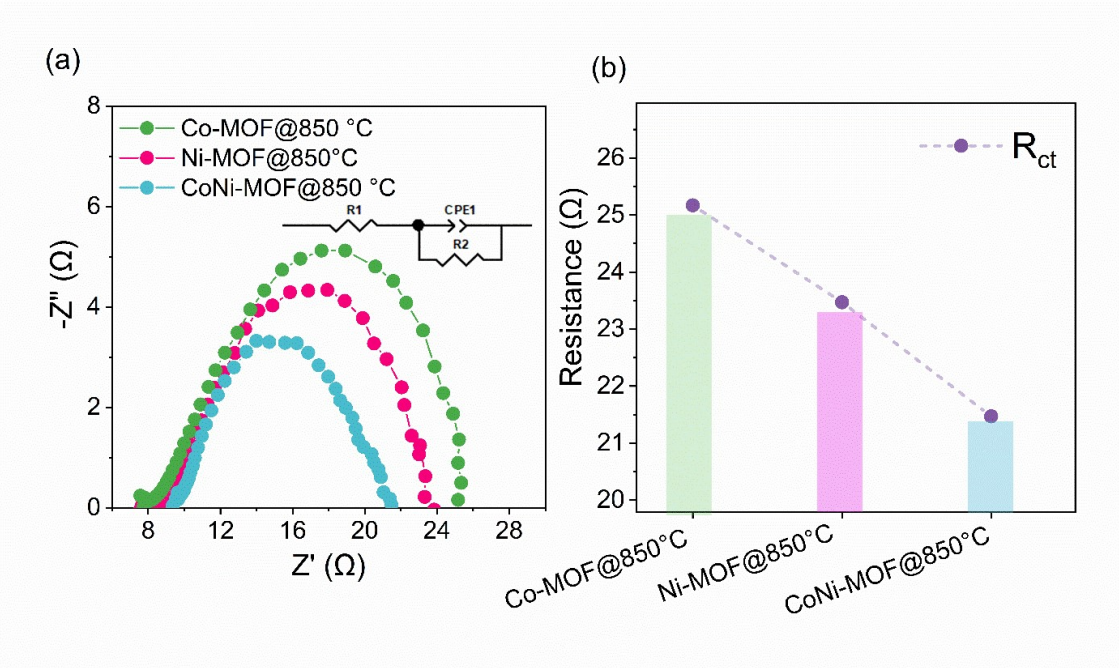


**Fig. S12** (a) Nyquist plots for Co-MOF@850°C, Ni-MOF@850°C, and CoNi-MOF850°C catalysts, and (b) $R_{ct}$ values for Co, Ni and CoNi catalysts.

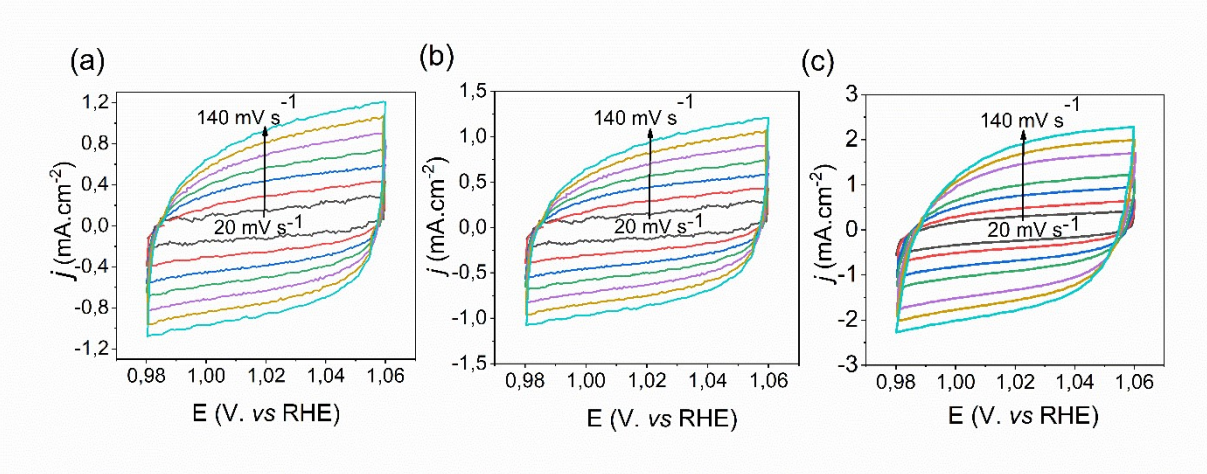


**Fig. S13** Cyclic voltammetry (CV) plot measured at different scan rates (20–140 mV s$^{-1}$) for (a) Co-MOF@850°C, (b) Ni-MOF@850°C and (c) CoNi-MOF@850°C catalysts.

The double-layer capacitance ($C_{dl}$) was evaluated using cyclic voltammetry (CV) at different scan rates (20–140 mV s$^{-1}$) within a potential window of 0.98–1.06 V vs. RHE. As the scan rate increased, the current density increased for Co, Ni and CoNi catalysts,

with CoNi-MOF@850°C exhibiting the highest current density. To determine the $C_{dl}$ value, the average capacitive current density (Δj) was calculated using Δj = |jc − ja|/2, where $j_c$ and $j_a$ represent the cathodic and anodic current densities, respectively. At a potential of 1.02 V, Δj was plotted against the scan rates, and the slope of the resulting linear fit provided the $C_{dl}$. Besides, the electrochemically active surface area (ECSA) of CoNi-MOF@850°C, calculated using ECSA = $C_{dl}/C_s$ (with Cs assed to be 0.02 mF/cm² in 1 M aqueous KOH), was determined to be 700.1 cm², significantly higher than that of Co-MOF@850°C (306.5 cm²) and Ni-MOF@850°C (364.5 cm²). This indicates that the Ni substitution generate more accessible active sites, thereby enhancing the overall catalytic performance.

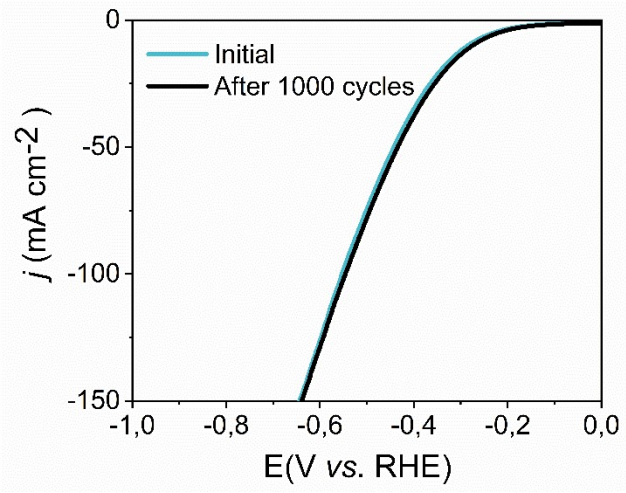


**Fig. S14** LSV curves of CoNi-MOF@850 °C catalyst recorded before and after 1000 CV cycles.

**Table. S4** Comparison of HER activity of Co-MOF@850 °C, Ni-MOF@850 °C, and CoNi-MOF@850 °C with other reported Co- and Co–Ni-based catalysts.

| Electrocatalyst | Overpotential (mV) | Tafel slope (mV $dec^{-1}$) | References |
|---|---|---|---|
| CoNi/NBC | 117 | 146 | [4] |
| $Ni_1Co_{10}$/C-oxide | 343 | 127 | [5] |
| CoNiO@CNC | 149 | 80 | [6] |
| Co-MOF-800 | 92 | 127 | [7] |
| CoNi-NCS | 260 | 122 | [8] |
| CoNiP/CoNi | 174 | 125 | [9] |
| XoNiP/CoNi-RGO | 150 | 97 | [10] |
| $Ni_{2.5}$-$Co_{2.5}$-Pn | 148 | 118 | [11] |
| $Co_x$-Niy-P | 130 | 93 | [12] |
| CoNi/$CoNiO_2$@NC-600 | 237 | 125 | [13] |
| CoNiP-NWs | 252 | 128 | [14] |
| $CoNiP_4O_{12}$ | 234 | 71.4 | [15] |
| $H_1$-NiCoP | 230 | 145 | [16] |
| CoS@CoNi-LDH/CC | 124 | 89 | [17] |
| Ni-Co-S | 129 | 96.1 | [18] |
| Ni doped $Co_3S_4$ | 270 | 97 | [19] |
| CoNi-MOF@NF | 147 | 109.6 | [20] |
| Co-MOF@850°C | 239 | 122 | This work |
| Ni-MOF@850°C | 172 | 116 | This work |
| CoNi-MOF@850°C | 148 | 65 | This work |

## 4. References


1. L. J. Farrugia, *Journal of Applied Crystallography*, 1999, 32, 837–838.
2. G. M. Sheldrick, *Acta Crystallographica Section C: Structural Chemistry*, 2018, 74, 2053–2296.
3. B. Ravel, M. Newville, *Journal of Synchrotron Radiation*, 2005, 12, 537–541.
4. M. R. Liu, Q. L. Hong, Q. H. Li, Y. Du, H. X. Zhang, S. Chen, T. Zhou, J. Zhang, *Advanced Functional Materials*, 2018, 28, 1805520.
5. X. Yang, Z. Li, Z. Yang, D. Meng, Z. Wang, *Catalysis Science & Technology*, 2024, 14, 6814–6823.
6. Z. Li, J. Wang, J. Zhang, C. Huang, J. J. Zhou, L. Xu, L. Wang, S. Lu, L. Chen, *Applied Surface Science*, 2024, 674, 159076.
7. A. Gupta, C. A. Allison, M. E. Ellis, J. Choi, A. Davis, R. Srivastava, F. M. de Souza, D. Neupane, S. R. Mishra, F. Perez, A. Kumar, T. Dawsey, *International Journal of Hydrogen Energy*, 2022, 47, 37684–37696.
8. Y. Lu, Y. Deng, S. Lu, Y. Liu, J. Lang, X. Cao, H. Gu, *Nanoscale*, 2019, 11, 21259–21265.
9. P. Arunkumar, S. Gayathri, J. H. Han, ChemSusChem, 2021, 14, 1921–1935.
10. Z. Cai, A. Wu, H. Yan, Y. Xiao, C. Chen, C. Tian, L. Wang, R. Wang, H. Fu, *Nanoscale*, 2018, 10, 7619–7629.
11. Y. Du, M. Zhang, Z. Wang, Y. Liu, Y. Liu, Y. Geng, L. Wang, *Journal of Materials Chemistry A*, 2019, 7, 8602–8608.
12. Q. Zhou, D. Wang, *New Journal of Chemistry*, 2022, 46, 7490–7496.
13. Q. Zhang, X. L. Li, B. X. Tao, X. H. Wang, Y. H. Deng, X. Y. Gu, L. J. Li, W. Xiao, N. B. Li, H. Q. Luo, *Applied Catalysis B: Environmental*, 2019, 254, 634–646.
14. I. Amorim, J. Xu, N. Zhang, D. Xiong, S. M. Thalluri, R. Thomas, J. P. S. Sousa, A. Araújo, H. Li, L. Liu, *Catalysis Today*, 2020, 358, 196–202.
15. B. Guo, J. Zhao, Y. Xu, X. Wen, X. Ren, X. Huang, S. Niu, Y. Dai, R. Gao, P. Xu, S. Li, *ACS Applied Materials & Interfaces*, 2024, 16, 8939–8948.
16. J. Zhang, L. Zhang, X. Wang, W. Zhu, Z. Zhuang, *Chemical Communications*, 2019, 56, 90–93.
17. K. Ao, Q. Wei, W. A. Daoud, *ACS Applied Materials & Interfaces*, 2020, 12, 33595–33602.
18. C. Wu, Y. Du, Y. Fu, W. Wang, T. Zhan, Y. Liu, Y. Yang, L. Wang, *Composites Part B: Engineering*, 2019, 177, 107252.
19. J. Wang, Y. Wang, Z. Yao, Z. Jiang, *Chinese Journal of Chemical Engineering*, 2022, 42, 380–388.
20. J. Chen, H. Zhang, Z. Shi, Q. Lu, Y. Feng, T. Zhang, *Ionics*, 2025, 31, 9419–9430.